Supporting information

Fine regulation of electron transfer in Ag@Co_3O_4 nanoparticles for boosting oxygen evolution reaction

Zhe Li,[†a] Yi Feng,[†a] Xiuyao Lang,[b] Wenjing Kang,[a] Jing Mao,[a] Gurong Shen,[a] Hui Liu,[a] Cunku Dong,[*a] Weichao Wang[*b] and Xiwen Du[*ac]

[a.] Institute of New Energy Materials, School of Materials Science and Engineering, Key Laboratory for Advanced Ceramics and Machining Technology of Ministry of Education, Tianjin University, Tianjin 300072, PR China.
Email: xwdu@tju.edu.cn (X.W. Du); ckdong@tju.edu.cn (C. K. Dong)

[b.] Department of Electronics, Tianjin Key Laboratory of Photo-Electronic Thin Film Device and Technology, Nankai University, Tianjin, 300071, PR China.
Email: weichaowang@nankai.edu.cn (W. C. Wang)

[c.] Longyan University, Longyan, 364012, PR China.

[†] Z. Li and Y. Feng contributed equally to this work.

EXPERIMENTAL SECTION

Synthesis of Ag nanoparticles. A colloidal solution of Ag nanoparticles was synthesized by pulsed laser ablation under the focused beam (laser beam energy: 200 mJ) of a Nd:YAG laser. A clean Ag target (99.99%, diameter: 20 mm, thickness: 5 mm) was immersed in deionized water (100 ml beaker), and the water surface is 10 mm from the upper surface of Ag target. Then the colloidal solution containing Ag nanoparticles could be obtained after 50 min of laser ablation.

Synthesis of Co_3O_4 nanoparticles. A colloidal solution of Co_3O_4 nanoparticles was synthesized by pulsed laser ablation under the focused beam (laser beam energy: 800 mJ) of a Nd:YAG laser. A clean Co target (99.99%, diameter: 20 mm, thickness: 5 mm) was immersed in deionized water (100 ml beaker), and the water surface is 10 mm from the upper surface of Co target. Then the colloidal solution containing Co_3O_4 nanoparticles could be obtained after 60 min of laser ablation.

Synthesis of different Ag@Co_3O_4 nanoparticles. The Ag@Co_3O_4 nanoparticles were prepared by electrostatic attraction and Ostwald ripening. The Ag nanoparticles colloidal solution and Co_3O_4 nanoparticles colloidal solution were mixed in different mass ratios (Ag : Co_3O_4 = 5.5 : 1 (ACO-1), 2.7 : 1 (ACO-2), 1.7 : 1 (ACO-3), 1.2 : 1 (ACO-4), 0.9 : 1 (ACO-5), 0.6 : 1 (ACO-6)), respectively. Then the mixed colloidal solutions were ultrasonically dispersed evenly for 60 min under the temperature of 25 °C. The mixed colloidal solutions were stirred under 50 °C for 10 h by magnetic stirring. The solutions were centrifuged (8000 rpm, 10 min), and then the different Ag@Co_3O_4 nanoparticles powder with various shell thickness (ACO-1 is 1.9 nm, ACO-2 is 3.6 nm, ACO-3 is 5.4 nm, ACO-4 is 7.3 nm, ACO-5 is 8.9 nm and ACO-6 is 11.6 nm) were obtained by vacuum freeze-dried.

Characterization. Transmission electron microscope (TEM) was taken using a JEOL 2100 TEM operated at 200 kV. X-ray diffraction (XRD) with Cu Kα radiation as the radiation source through a Ni filter (Bruker D8 Advanced) was used to determine the crystalline structure of the catalysts. Raman spectra was acquired on inVia reflex (RENISHAW) at an excitation wavelength of 532 nm (spectral resolution: < 1 cm^{-1}, spectral repeatability: 0.15 cm^{-1}). The zeta potential analysis was conducted at 25 °C using Malvern Zetasizer Nano-ZS90 (UK). XPS analysis was measured by a THERMO SCIENTIFIC ESCALAB 250Xi.

Synchrotron-based sXAS measurement. The sXAS measurements were oprated at the BL08U1A beamline of the Shanghai Synchrotron Radiation Facility (SSRF). The photon energy of the spectroscopic microbeam line station (BL08U1A) of Shanghai Light Source is optimized between 250 eV and 2000 eV. The Energy resolution (ΔE / E) is 10 000@244 eV, 7400@410 eV. The Photon flux at sample is 1.5 × 10^8 phs/s@244 eV@200 mA and 1.1 × 10^8 phs/s@1840 eV@200 mA in 30 nm spot. The scanning transmission X-ray microscopy (STXM) of the line station combines high spatial resolution (better than 30nm) and high chemical state resolution capabilities of near-edge absorption fine structure spectroscopy (NEXAFS), which can study solids at the sub-micron scale Characteristics.

Electrochemical measurement. The OER activity of different Ag@Co_3O_4 nanoparticles was measured using electrochemical workstation CHI660E (reference electrode: KCl-saturated Hg/Hg_2Cl_2, counter electrode: graphite rod). Glassy carbon was used as working electrode (area: 0.07 cm^2). 6 mg carbon black and 4 mg catalyst powders were suspended in 20 µl Nafion solution (5 wt.%, Du Pont), 500 µl deionized water and 500 µl isopropanol to obtain a homogeneous ink. Quantitative ink was spread on working electrode. The loading of catalysts is 0.4 mg/cm^2. 30 CVs were performed at 50 mV s^{-1} before polarization curve test.

Theoretical calculation. All DFT calculations used normal dipole correction to eliminate the pseudo-electrostatic interaction between adjacent slabs. The U-J term is 1.9 eV for Co and equilibrium lattice constant was calculated to be 8.04 Å for anti-ferromagnetic bulk Co_3O_4 with an energy gap of 1.48eV, which is in agreement with the previous study. For theoretical simulation of interface, we choose Ag (111) (*Nat. Cata. 2019, 2, 134-141. Nat. Cata. 2019, 2, 1107-1114.*) and Co_3O_4 (111) (*Adv. Funct. Mater. 2019, 29, 1903444. ACS Appl. Mater. Interfaces 2017, 9, 27736-27744.*) planes which match each other very well and can form a stable interface.

		Ag(111) P(2*2)	**Co_3O_4(111) P(1*1)**
Lattice constant (Å)	**a**	5.875	5.682
	b	5.875	5.682

Slab models of Co_3O_4 (111) surfaces with different Co terminations were utilized. The lower surface of Co_3O_4 (111) was passivated with pseudohydrogen to make the lower surface band gap 1.48eV. The lower surface of Co_3O_4 (111) formed an interface with four layers of silver, and the interface was silver-cobalt bonding. During surface relaxation, only the bottom layer of Ag is fixed, while all four layers of silver were fixed in the calculations of the adsorption processes. The computational hydrogen electrode (CHE) was used to simulate the electrochemical reaction properties. Gibbs free energy changes (ΔG) were calculated by $\Delta G = \Delta E + \Delta ZPE - T\Delta S$ (ΔE: energy difference, ΔZPE: changes in zero-point energy, ΔS: changes in zero-point entropy). Zero-point entropy and energy are obtained from the vibration frequency calculations and NIST database (T=300K), separately.

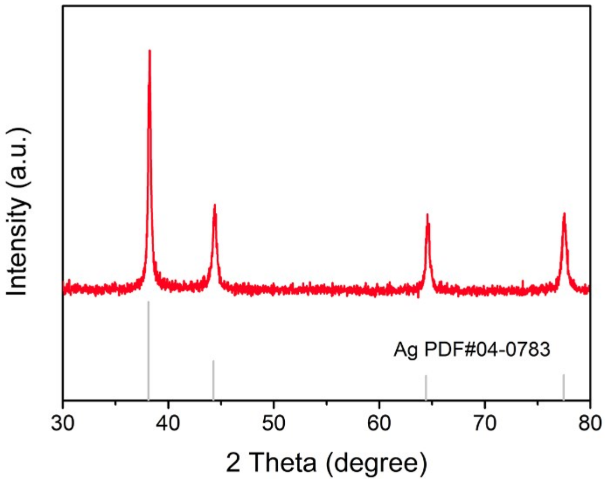

Fig. S1 The XRD pattern of Ag nanoparticles derived from PLAL.

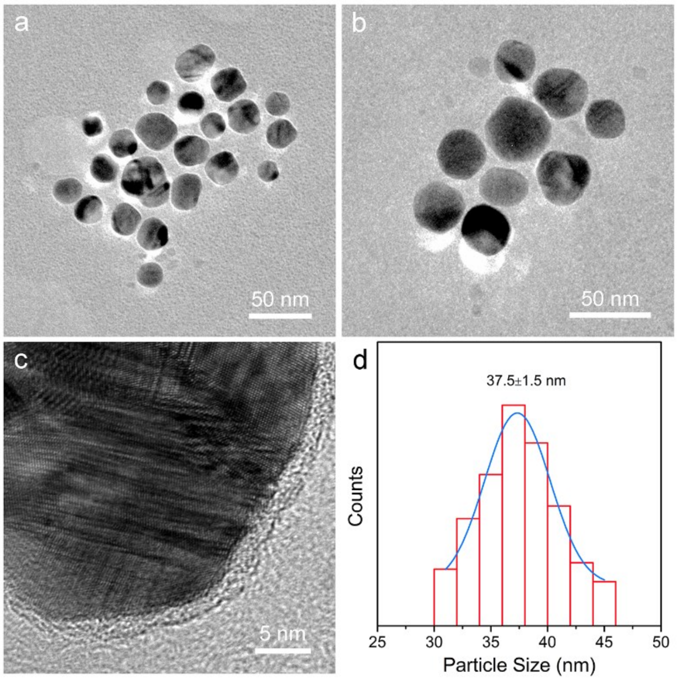

Fig. S2 Characterization of Ag nanoparticles derived from PLAL. (a) - (c) TEM images of Ag nanoparticles. (d) Size distribution pattern of Ag nanoparticles.

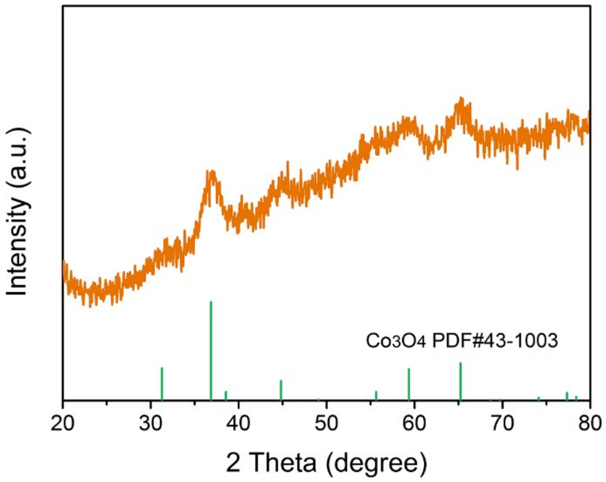

Fig. S3 The XRD pattern of Co_3O_4 nanoparticles derived from PLAL.

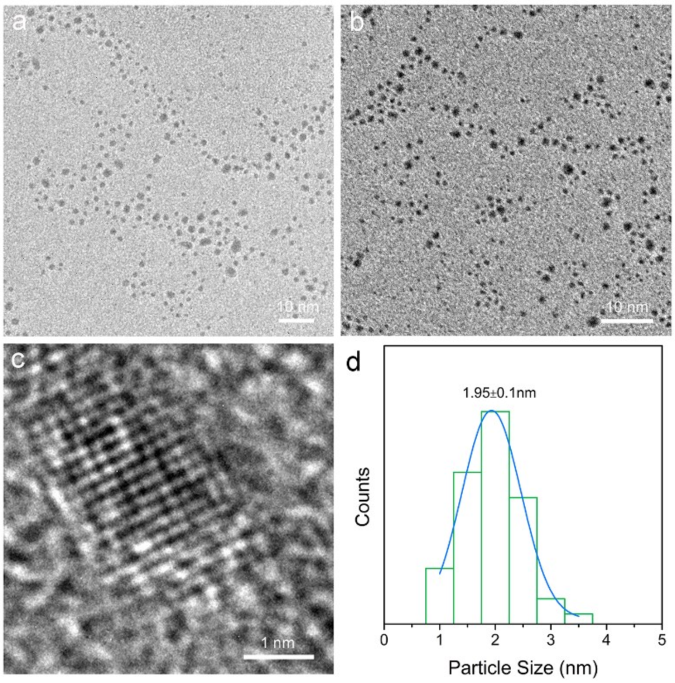

Fig. S4 Characterization of Co_3O_4 nanoparticles derived from PLAL. (a) and (b) TEM images of Co_3O_4 nanoparticles. (c) Size distribution pattern of Co_3O_4 nanoparticles.

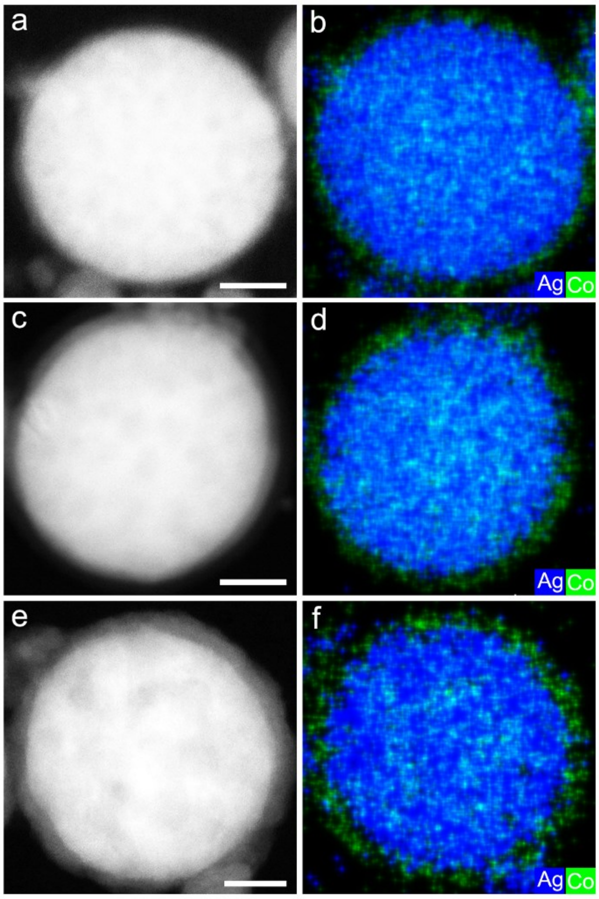

Fig. S5 X-ray energy dispersive spectroscopy (EDS) mapping images of Ag@Co_3O_4 core-shell nanoparticle. (a) HAADF image of ACO-1 nanoparticle. (b) EDS-mapping image of ACO-1 nanoparticle. (c) HAADF image of ACO-2 nanoparticle. (d) EDS-mapping image of ACO-2 nanoparticle. (e) HAADF image of ACO-3 nanoparticle. (f) EDS-mapping image of ACO-3 nanoparticle.

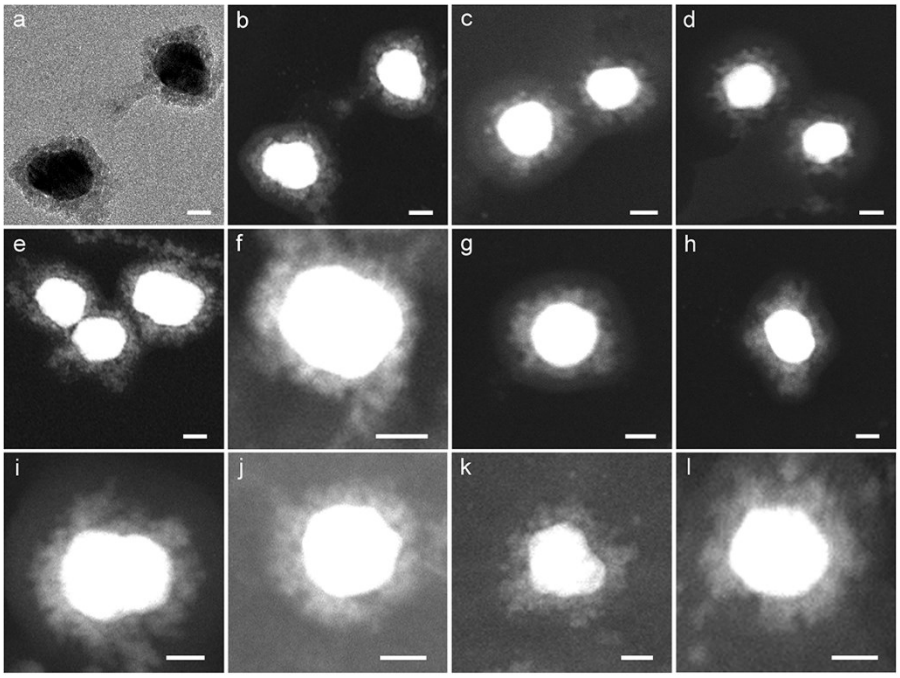

Fig. S6 TEM characterization of Ag@Co_3O_4 core-shell nanoparticle. (a) TEM image of ACO-4 nanoparticle. (b) HAADF image of ACO-4 nanoparticle in (a). (c) – (d) HAADF images of ACO-4 nanoparticle. (e) – (h) HAADF images of ACO-5 nanoparticle. (i) – (l) HAADF images of ACO-6 nanoparticle. The scale bar is 20 nm.

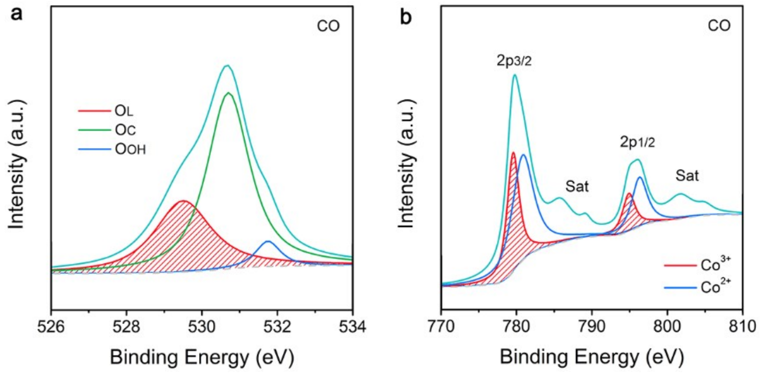

Fig. S7 XPS characterization of CO nanoparticles. (a) O1s spectra. (b) Co 2p spectra. O_L is the lattice oxygen, O_C is the chemisorbed oxygen species, O_{OH} is the oxygen in hydroxyl of physically adsorbed H_2O.

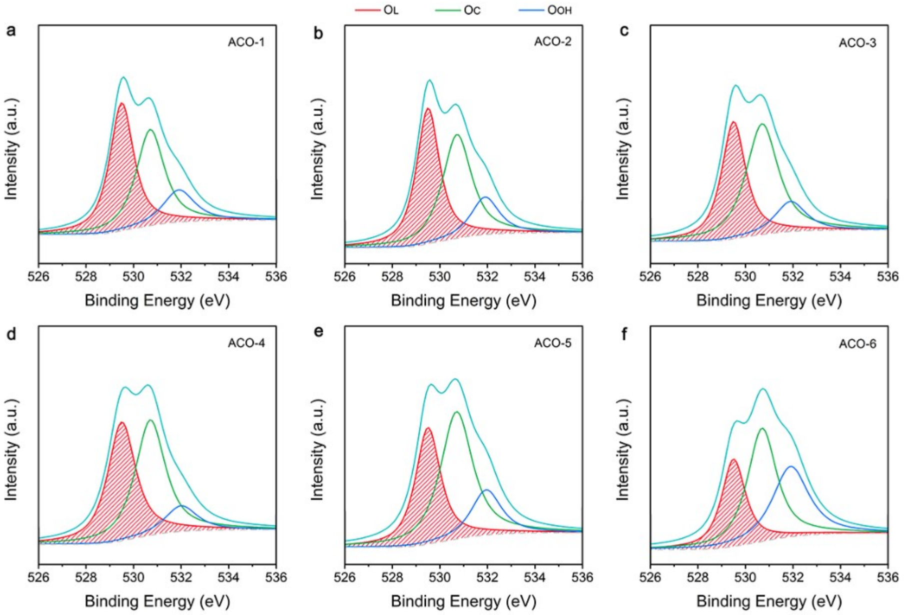

Fig. S8 O1s XPS spectra of different Ag@Co_3O_4 nanoparticles. (a) ACO-1. (b) ACO-2. (c) ACO-3. (d) ACO-4. (e) ACO-5. (f) ACO-6. O_L is the lattice oxygen, O_C is the chemisorbed oxygen species, O_{OH} is the oxygen in hydroxyl of physically adsorbed H_2O.

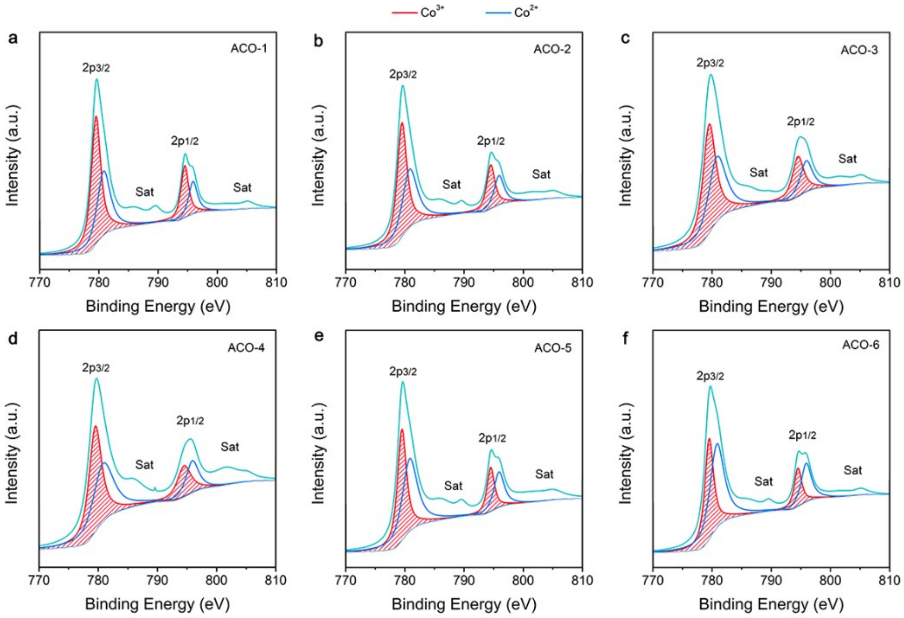

Fig. S9 Co 2p XPS spectra of different Ag@Co_3O_4 nanoparticles. (a) ACO-1. (b) ACO-2. (c) ACO-3. (d) ACO-4. (e) ACO-5. (f) ACO-6.

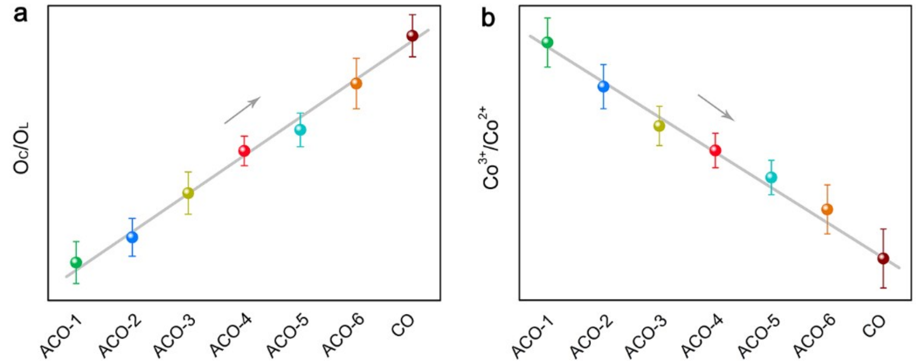

Fig. S10 O_C/O_L and Co^{3+}/Co^{2+} comparison of different Ag@Co_3O_4 nanoparticles. (a) O_C/O_L. (b) Co^{3+}/Co^{2+}. The ratio of O_C and O_L represents the content of oxygen vacancy.

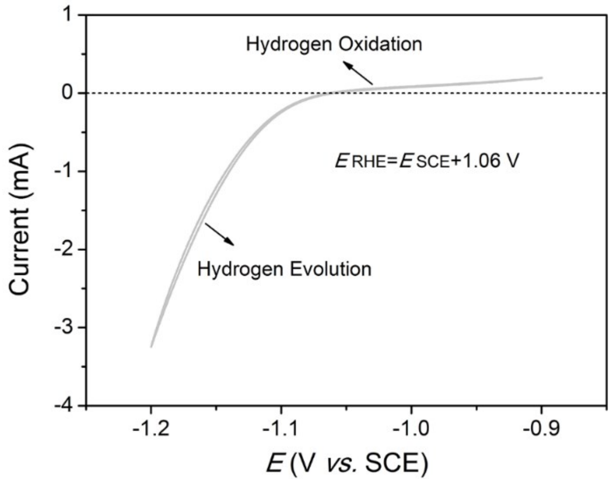

Fig. S11 Calibration of the reference saturated calomel electrode (SCE). The calibration was performed in hydrogen saturated electrolyte with a Pt sheet as the working electrode and counter electrode. Cyclic voltammetry runs at a scan rate of 1 mV/s. In 1M KOH, the $E_{RHE}=E_{SCE}+1.06$ V.

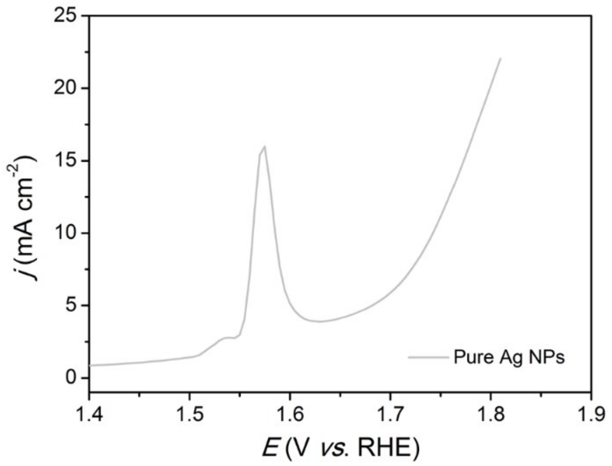

Fig. S12 The OER polarization curve of Ag nanoparticles in O_2-saturated 1 M KOH aqueous electrolyte.

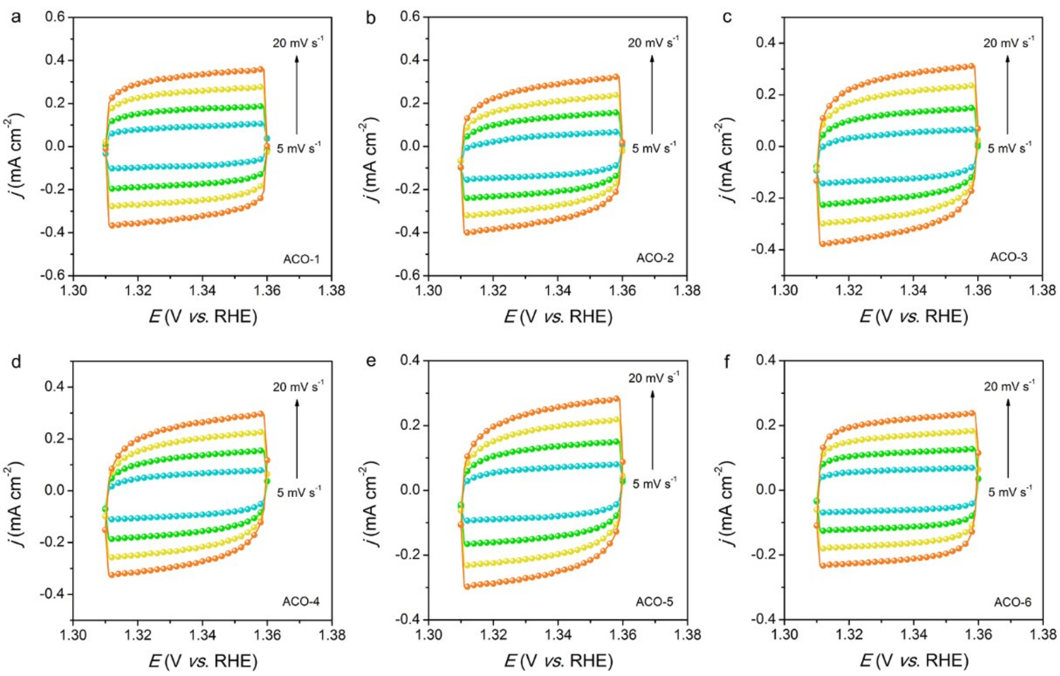

Fig. S13 Double layer capacitance (Cdl) tests in 1M KOH by Cyclic voltammetry (CV). CV curves were tested at different scan rate of 5 mV/s, 10 mV/s, 15 mV/s and 20 mV/s in the potential range of the OER reaction (1.31 V ~ 1.36 V vs. RHE). (a) ACO-1. (b) ACO-2. (c) ACO-3. (d) ACO-4. (e) ACO-5. (f) ACO-6.

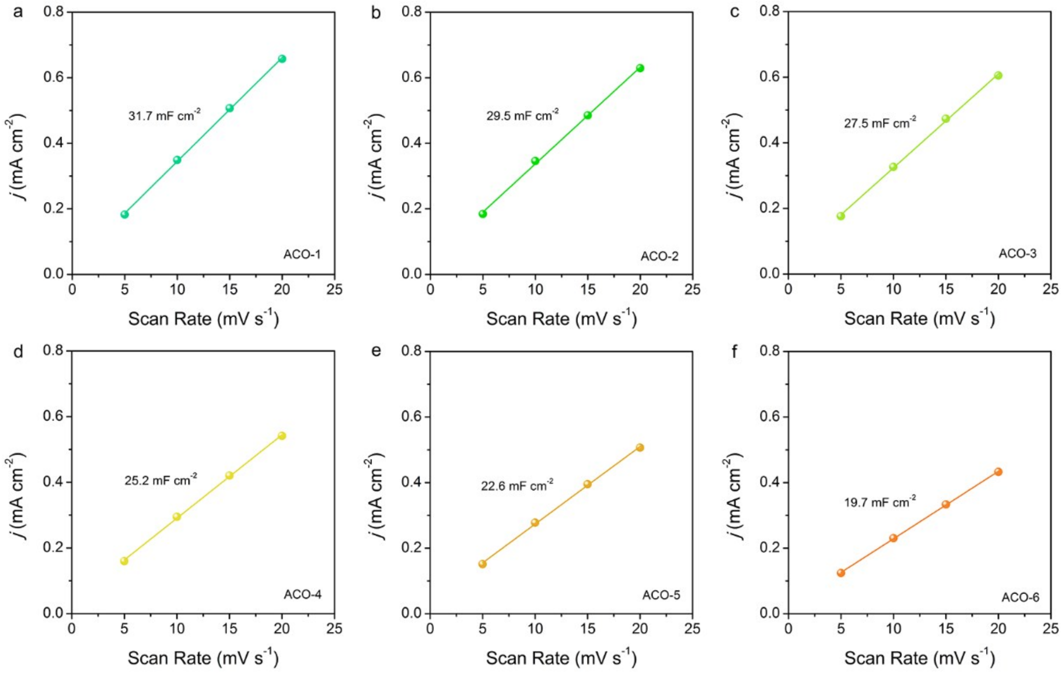

Fig. S14 Double layer capacitance (Cdl) calculated from CV curves. (a) Plot of the current density versus the scan rate of ACO-1. (b) Plot of the current density versus the scan rate of ACO-2. (c) Plot of the current density versus the scan rate of ACO-3. (d) Plot of the current density versus the scan rate of ACO-4. (e) Plot of the current density versus the scan rate of ACO-5. (f) Plot of the current density versus the scan rate of ACO-6.

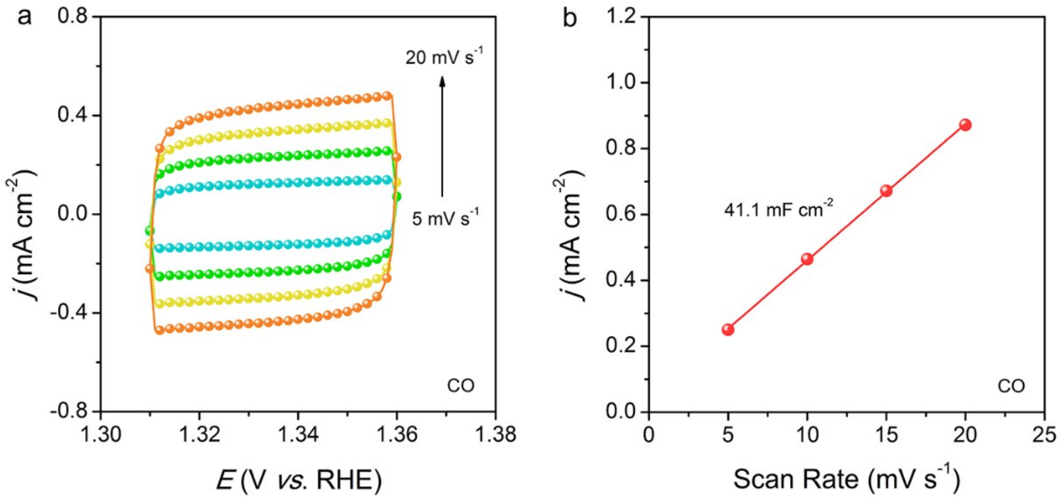

Fig. S15 Double layer capacitance (Cdl) of CO tested in 1M KOH by Cyclic voltammetry (CV). (a) CV curves were tested at different scan rate of 5 mV/s, 10 mV/s, 15 mV/s and 20 mV/s in the potential range of the OER reaction (1.31 V ~ 1.36 V vs. RHE). (b) Plot of the current density versus the scan rate of ACO-1.

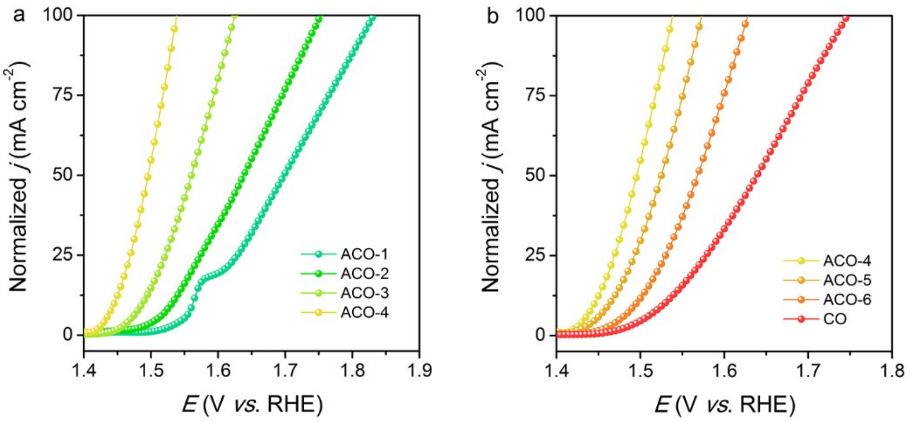

Fig. S16 The OER polarization curves normalized by ECSA in O_2-saturated 1 M KOH aqueous electrolyte. (a) OER polarization curves of ACO-1, ACO-2, ACO-3 and ACO-4. (b) OER polarization curves of ACO-4, ACO-5, ACO-6 and CO.

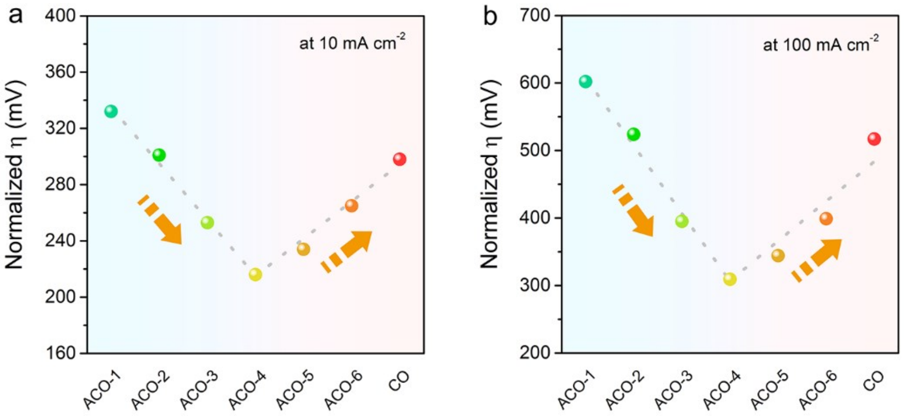

Fig. S17 The comparison of OER performance derived from polarization curves normalized by ECSA. (a) Volcano curve between experimental overpotential (at 10 mA cm^{-2}) and different Co_3O_4 samples with the continuously varying valence state of Co ions. (b) Volcano curve between experimental overpotential (at 100 mA cm^{-2}) and different Co_3O_4 samples with the continuously varying valence state of Co ions. The gray lines are shown to guide the eye.

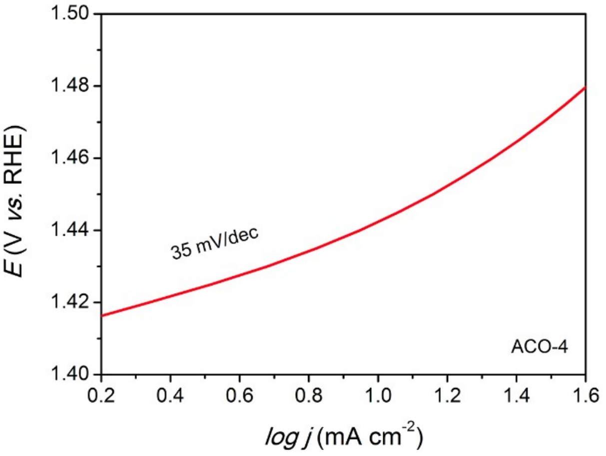

Fig. S18 The OER Tafel plot of ACO-4 catalyst in O_2-saturated 1 M KOH aqueous electrolyte.

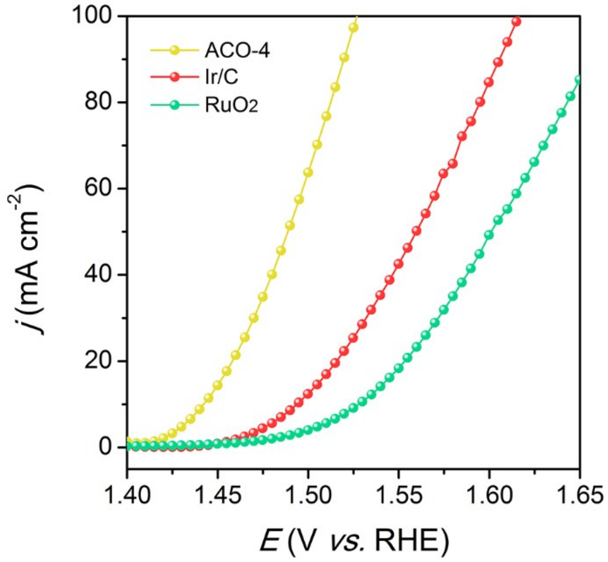

Fig. S19 Polarization curves of ACO-4, commercial Ir/C and commercial RuO_2 catalysts.

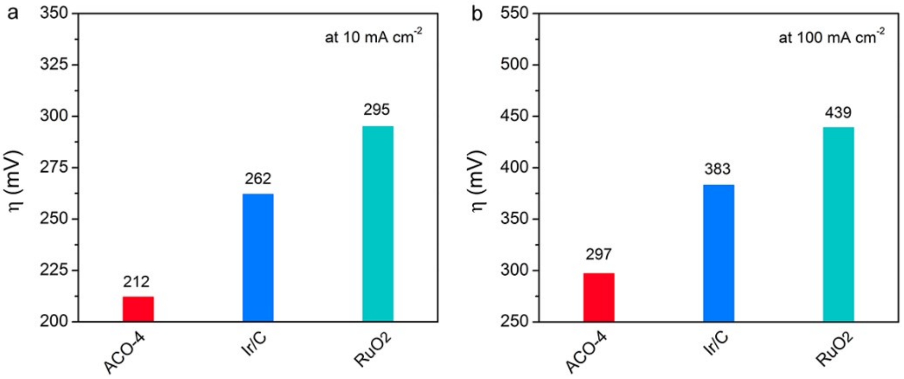

Fig. S20 The OER activity comparison between ACO-4 and commercial Ir/C, RuO_2 at 10 mA cm^{-2} (a) and 100 mA cm^{-2} (b) in O_2-saturated 1 M KOH aqueous electrolyte.

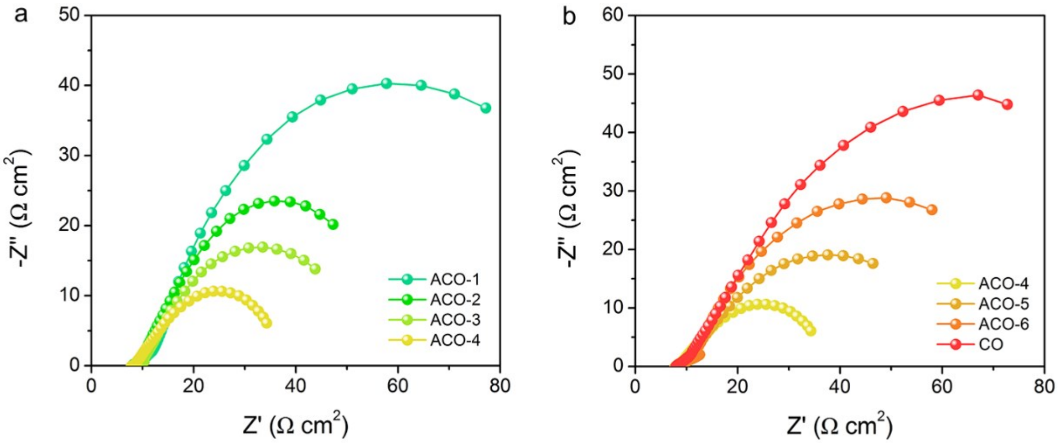

Fig. S21 Electrochemical impedance spectroscopy (EIS) tests in O_2-saturated 1 M KOH aqueous electrolyte. (a) EIS of ACO-1, ACO-2, ACO-3 and ACO-4. (b) EIS of ACO-4, ACO-5, ACO-6 and CO.

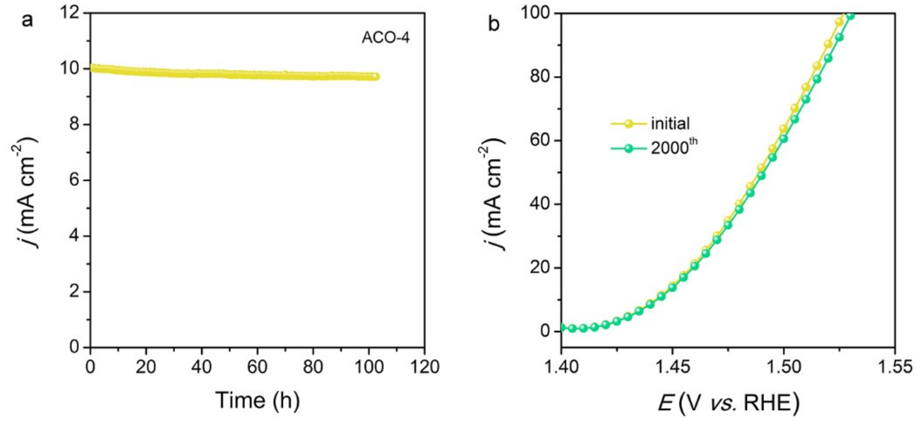

Fig. S22 (a) The OER catalytic stability of ACO-4 by 100 h continuous i-t test. (b) The OER catalytic stability of ACO-4 by CV accelerated durability test.

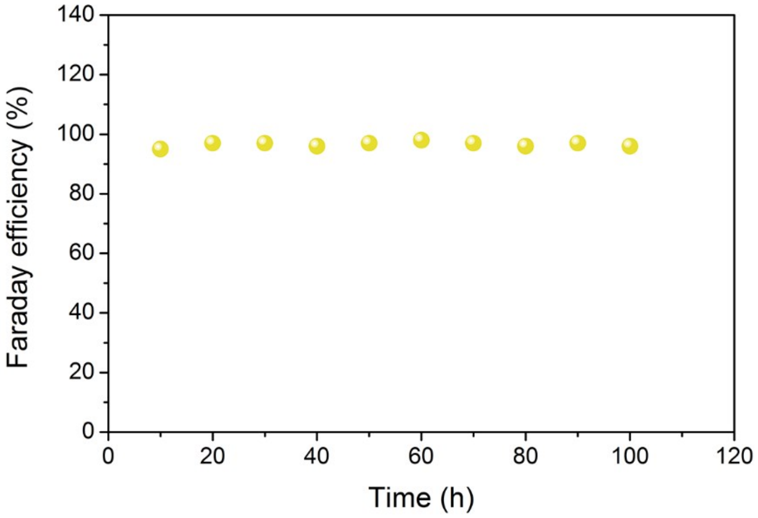

Fig. S23 Oxygen evolution Faraday efficiency for ACO-4 in 100 hours continuous test.

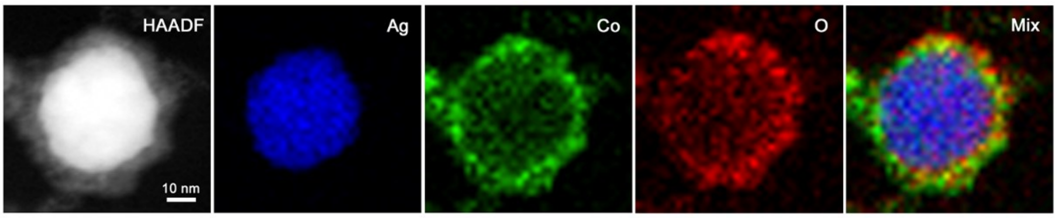

Fig. S24 HAADF-STEM and EDS-mapping images of ACO-4 nanoparticle after OER stability test.

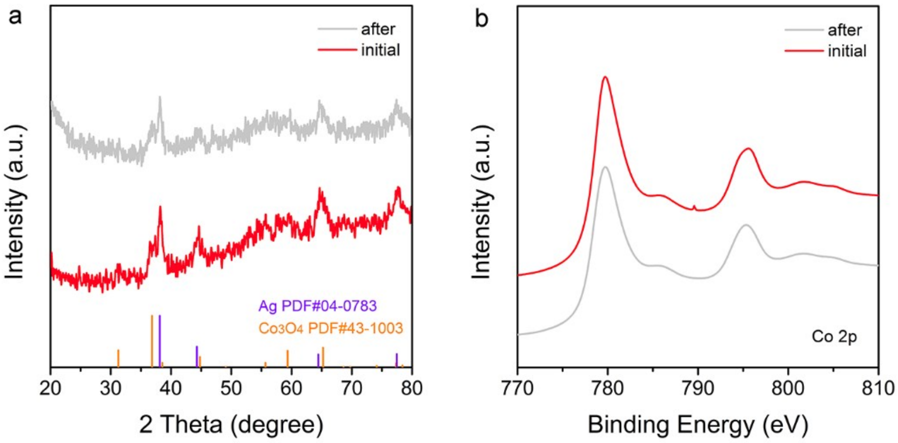

Fig. S25 XRD pattern (a) and Co 2p XPS spectra (b) of ACO-4 nanoparticle after OER stability test.

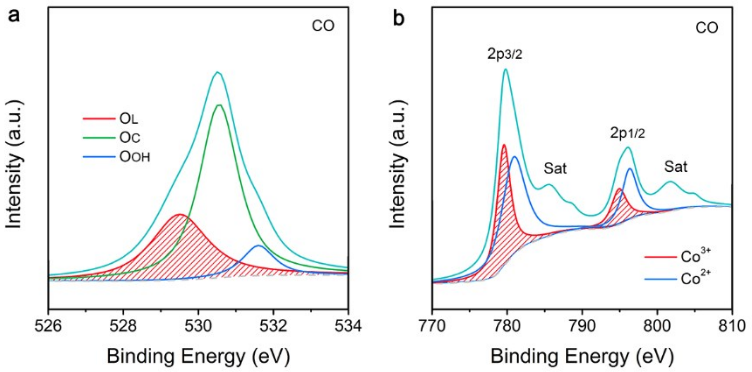

Fig. S26 XPS characterization of CO nanoparticles after OER test. (a) O1s spectra. (b) Co 2p spectra. O_L is the lattice oxygen, O_C is the chemisorbed oxygen species, O_{OH} is the oxygen in hydroxyl of physically adsorbed H_2O.

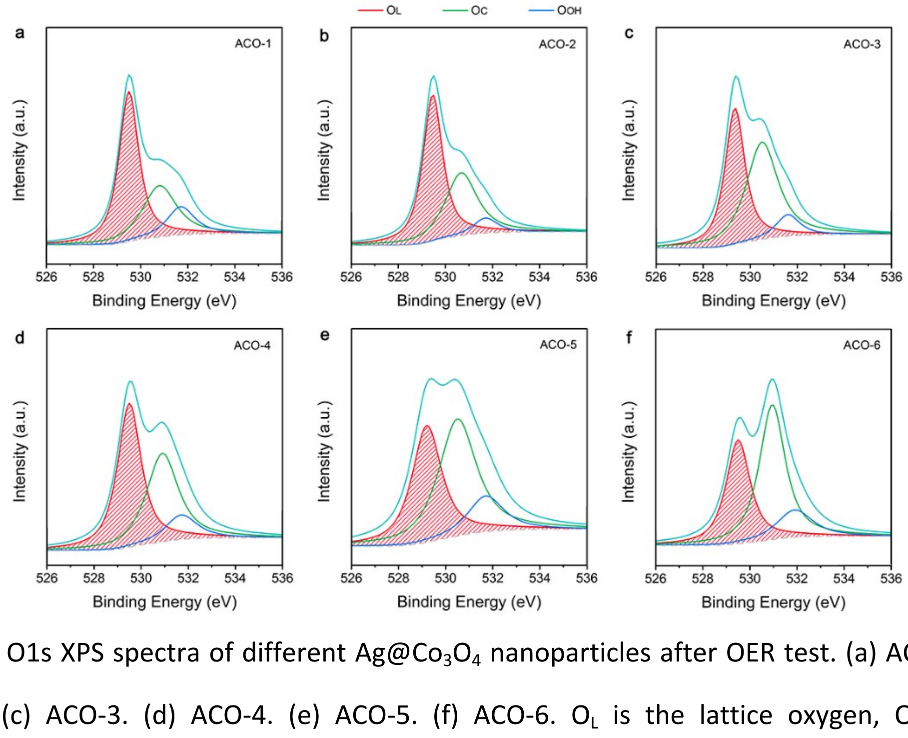

Fig. S27 O1s XPS spectra of different Ag@Co_3O_4 nanoparticles after OER test. (a) ACO-1. (b) ACO-2. (c) ACO-3. (d) ACO-4. (e) ACO-5. (f) ACO-6. O_L is the lattice oxygen, O_C is the chemisorbed oxygen species, O_{OH} is the oxygen in hydroxyl of physically adsorbed H_2O.

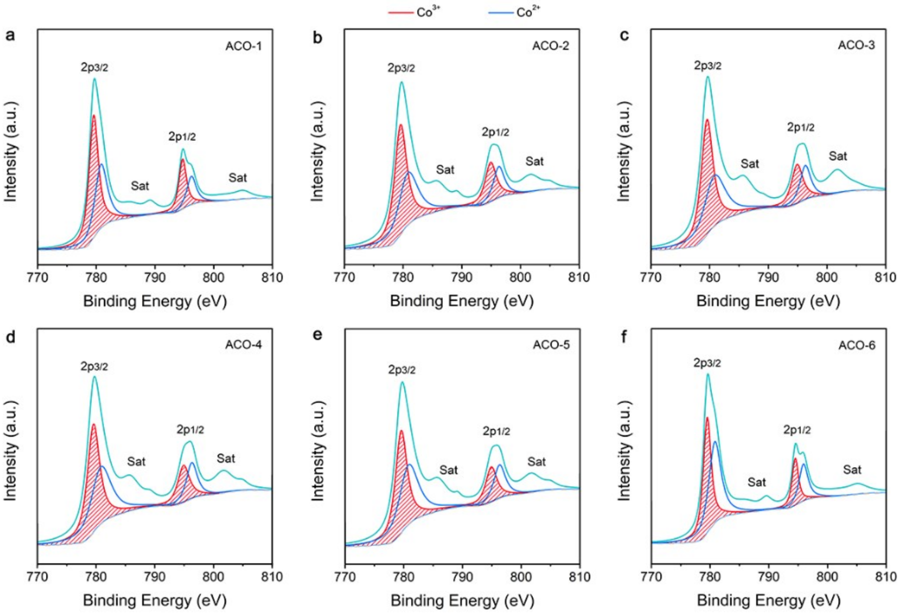

Fig. S28 Co 2p XPS spectra of different Ag@Co_3O_4 nanoparticles after OER test. (a) ACO-1. (b) ACO-2. (c) ACO-3. (d) ACO-4. (e) ACO-5. (f) ACO-6.

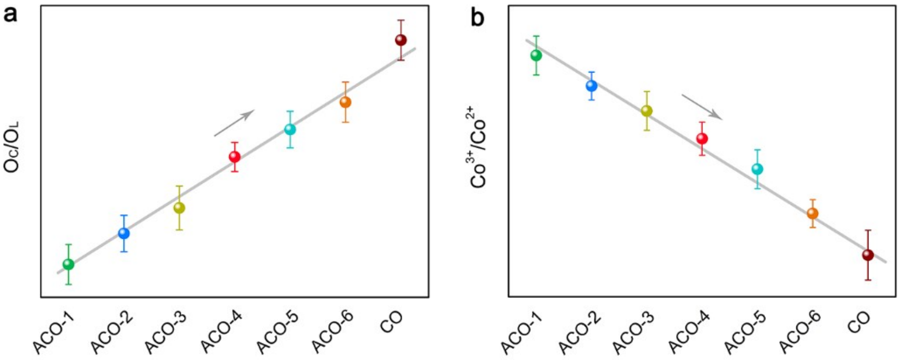

Fig. S29 O_C/O_L and Co^{3+}/Co^{2+} comparison of different Ag@Co_3O_4 nanoparticles after OER test. (a) O_C/O_L. (b) Co^{3+}/Co^{2+}. The ratio of O_C and O_L represents the content of oxygen vacancy.

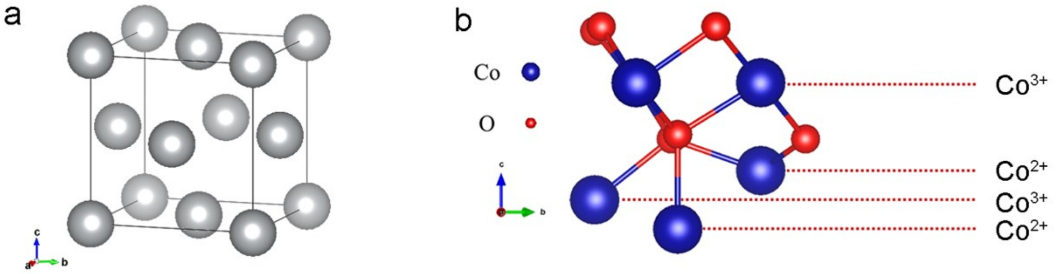

Fig. S30 Theoretical calculation atomic models. (a) Ag atomic model. (b) Co_3O_4 atomic model.

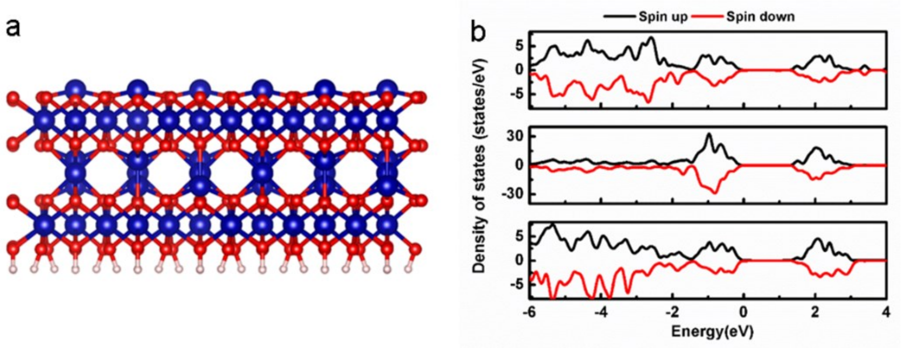

Fig. S31 The passivation of Co_3O_4 lower surface. (a) The passivation atomic model of Co_3O_4. (b) Density of states for Co_3O_4 after passivation.

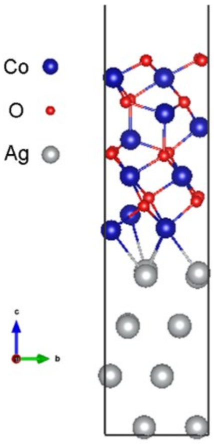

Fig. S32 Theoretical calculation atomic model of the interface between Ag and Co_3O_4.

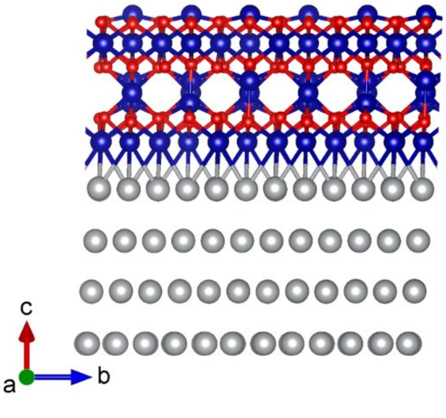

Fig. S33 The blank theoretical calculation atomic model of the interface between Ag and Co_3O_4 in the calculation of charge density distribution.

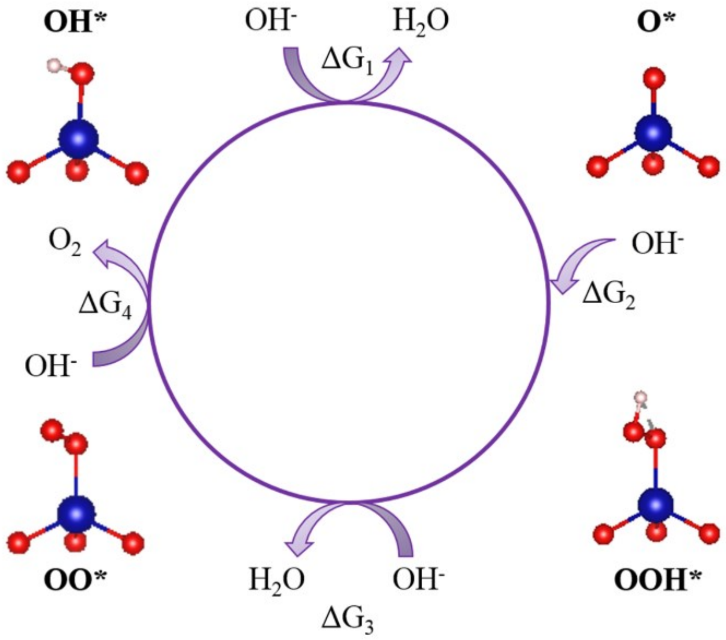

Fig. S34 The scheme of the proposed OER mechanism on Co_3O_4. The OER process occurs following the pathway:

$$(1) \quad OH^* + OH^- \rightarrow OH^* + H_2O + e^-$$

$$(2) \quad O^* + OH^- \rightarrow OOH^* + e^-$$

$$(3) \quad OOH^* + OH^- \rightarrow OO^* + H_2O + e^-$$

$$(4) \quad OO^* + OH^- \rightarrow OH^* + O_2(g) + e^-$$

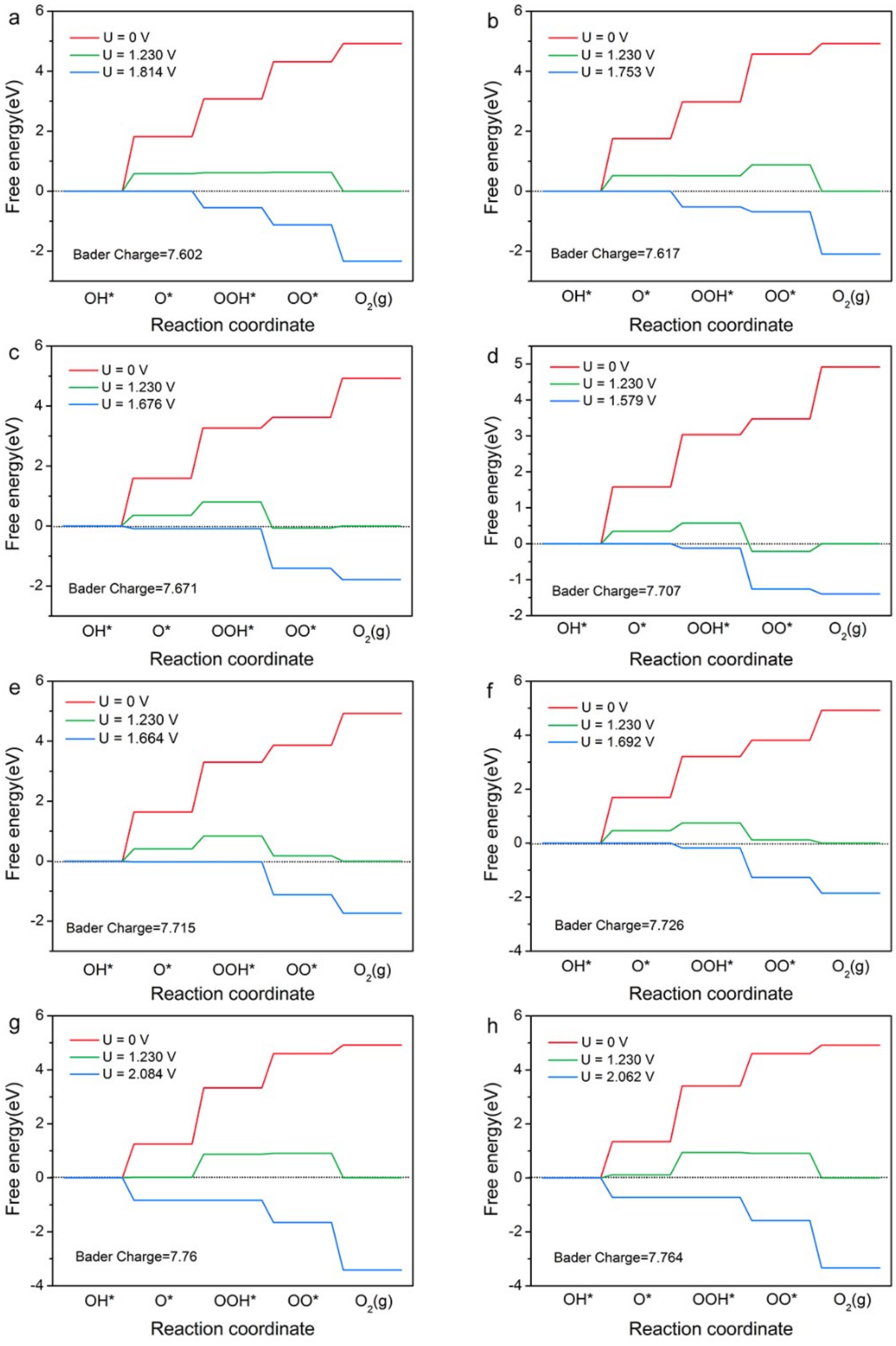

Fig. S35 The calculated OER free energy diagrams on catalytic sites with different Co bader charge.

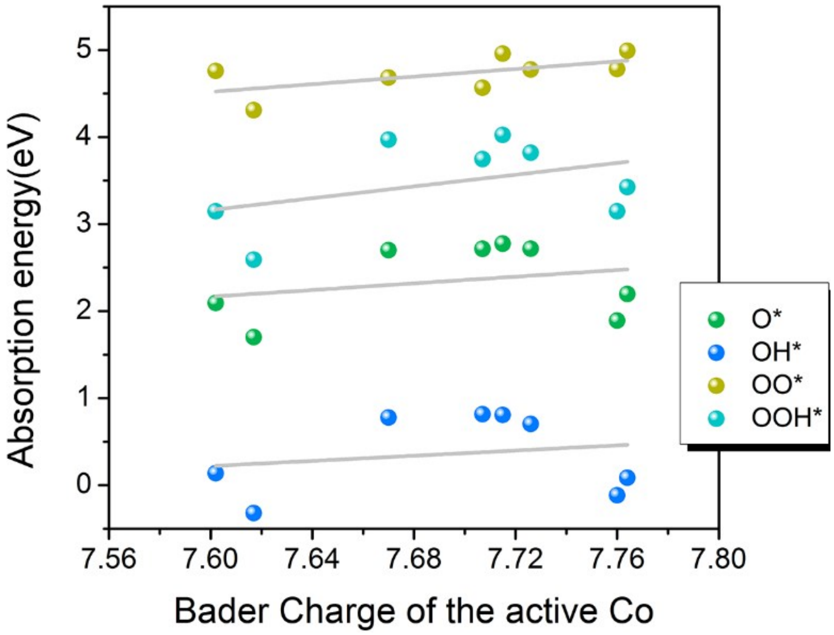

Fig. S36 The calculated absorption energy of different reaction intermediates on catalytic sites with different Co bader charge.